

LAAT: Locally Aligned Ant Technique for detecting manifolds of varying density*

Abolfazl Taghribi[†], Kerstin Bunte¹, Rory Smith², Jihye Shin², Michele Mastropietro³, Reynier F. Peletier⁴, and Peter Tino⁵

¹Faculty of science and engineering, University of Groningen, Netherlands

²Korea Astronomy and Space Science Institute

³Ghent University

⁴Kapteyn astronomical institute, University of Groningen, Netherlands

⁵School of Computer Science, University of Birmingham

September 18, 2020

Abstract

Dimensionality reduction and clustering are often used as preliminary steps for many complex machine learning tasks. The presence of noise and outliers can deteriorate the performance of such preprocessing and therefore impair the subsequent analysis tremendously. In manifold learning several studies indicate solutions for removing background noise or noise close to the structure when the density is substantially higher than that exhibited by the noise. However, in many applications, including astronomical datasets, the density varies alongside manifolds that are buried in a noisy background. We propose a novel method to extract manifolds in the presence of noise based on the idea of Ant colony optimization. In contrast to the existing random walk solutions, our technique captures points which are locally aligned with major directions of the manifold. Moreover, we empirically show that the biologically inspired formulation of ant pheromone reinforces this behavior enabling it to recover multiple manifolds embedded in extremely noisy data clouds. The algorithm's performance is demonstrated in comparison to state-of-the-art approaches, such as Markov Chain, LLPD and Disperse, on several synthetic and real astronomical datasets stemming from an N-body simulation of a cosmological volume.

Keywords— Ant algorithm, Markov Chain, multiple manifold detection, evolutionary computation

1 Introduction

Many fields such as astronomy [1], genetics [2, 3], medical science [4, 5], and sensory activity recognition [6] deal with a large number of high-dimensional data points located on some lower-dimensional structure hidden inside big data point clouds. Nonlinear dimensionality reduction methods [7] and manifold learning techniques [8] try

to find the underlying low dimensional manifold and project the data on a lower-dimensional space to save computation in the next steps of analyzing the data. However, in real-world applications, sample points may exist on several to many linear or nonlinear manifolds surrounded by noise and outliers which depreciate the result of conventional nonlinear dimensionality reduction methods [8]. Besides, these manifolds might intersect with each other [1].

The presence of noise and outliers is known to affect the results of manifold learning and dimensionality reduction techniques [8, 9]. Several solutions for denoising manifolds, such as structure-aware data consolidation [8] and manifold denoising [9] do not remove any points but move the points toward the manifolds. These techniques improve the results of clustering or manifold learning as long as the noise points are close to the points on the manifolds. However, noise points or outliers in the background far away from the manifolds are not distinguishable by them. Several papers have addressed the problem of manifold denoising and discover manifolds specifically for astronomical datasets [1, 10, 11, 12]. In [11, 12], and [10] the one-dimensional manifolds are detected based on topological structure and Delaunay tessellation of the data. These techniques do not specify the points belonging to one-dimensional manifolds, but they determine the position of the medial axis. Furthermore, extensions of these methods to higher dimensions increases the computational costs rapidly.

Noise also deteriorates the results of clustering techniques. The Longest Leg Path Distance (LLPD) [13] was proposed as a new metric for elongated noisy clusters. If the value of the LLPD metric from a point to its neighbors is larger than a predetermined threshold, the point is recognized as noise and hence removed from the dataset for the next steps. Later, in [13] it was shown that spectral clustering [14] benefits from using the LLPD metric for clustering data with elongated clusters. However, it provides no solution if clusters are highly curved and of different size. Outliers are problematic for multiple manifold clustering as stated by [15, 16]. Both approaches show limitations when large numbers of noise points are present. The latter suggests to handle this problem by removing outliers only if they constitute a small fraction of the number of inliers, stating that the method is not extendible to a large number of noise points. Graph-based methods combined with Markov chain have been also used for clustering and dimensionality reduction, with approaches mostly based on computation of several dominant eigenvectors [7, 17, 18].

*This work has been submitted to the IEEE for possible publication. Copyright may be transferred without notice, after which this version may no longer be accessible.

[†]abolfazl.taghribi@gmail.com

Nonetheless, on datasets with a large number of samples building the transition matrix and computing the eigenvectors is both memory and time-consuming. Even methods such as Arnoldi iterations [19] requires a substantial computation to estimate dominant eigenvectors. Besides, these methods consider the case of single or multiple manifolds in a medium without noise [17, 20], which is not true in many physical applications, such as in cosmological simulations [1].

The problem of identifying noise points in large datasets and detecting manifolds with high probability can be viewed as an optimization problem with the aim of exploring all points in a dataset and spotting the ones which are embedded in a specific structure. From this point of view, it is similar to a standard swarm optimization problem where the aim is to discover the shortest path between all possible routes. The ant system [21] and ant colony system [22] are two heuristic methods applied to problems including the traveling salesman, vehicle routing and job scheduling. There have also been several studies on using ant colony optimization for clustering. These methods can be accurate [23, 24], and they have been designed to deal with a modest amounts of outliers [25]. Nevertheless, as they often consider the Euclidean distance between points to decide whether they belong to one cluster or not, they are not capable of denoising manifolds with high curvature. Moreover, since they are computationally demanding, processing large quantities of data may be infeasible. Accordingly, the problem of clustering and manifold detection in the presence of noise needs more investigation.

In this contribution we propose a novel method, extending the ant colony algorithm, able to remove noise from large point clouds and capture multiple manifolds buried within. We demonstrate that depositing pheromone and an pheromone evaporation mechanisms is useful and effective in finding the points on the manifold and ignoring outliers. Our experiments confirm that the alignment between the direction of the jump and the manifold tangent vector outperforms using the Euclidean distance between a point and its neighbors as bases for the decision of the ant’s jumping preference. Additionally, we demonstrate the result of the proposed method on real astronomical data with 6.7 million samples, showing that our method is capable of separating the data into meaningful parts. Note that our method is neither a clustering nor a manifold learning method, but rather a denoising strategy that improves the result of such techniques in multiple scenarios: 1) facing a large number of outliers, 2) multiple clusters or nonlinear manifolds, and 3) of potentially varying noise within and across the structures. We also note that our approach does not address the detection and learning of lower-dimensional structures as done in image processing and computer vision communities [26]. There, the emphasis is on capturing a limited number of natural degrees freedom that often characterizes image collections or video streams. In contrast, we aim to zoom on potentially intricately related complex low-dimensional manifold structures embedded in spaces of much lower dimension than that of the image spaces.

The paper is organized as follows. In section 2 we introduce our extended ant algorithm for extracting manifolds from noisy point clouds and its theoretical foundation. Section 3 explains the synthetic and astronomical datasets that are then used to demonstrate the parameter robustness and performance of our method¹ in comparison with previous work. A concrete example demonstrating the application of the method to higher dimensional data is given in section 5 and in 6 the paper finally concludes and provides directions for future work.

2 Extracting manifolds using the ant colony

The ant colony algorithm is mostly used to detect the shortest path between the original starting point and the destination, where there are many routes between these two points. Generally such ant colony algorithms implement a random walk procedure in which simulated ants move from point to point in search of a reward (the artificial counterpart to food) guided by two factors:

1. the heuristic for choosing the shortest path, which is sometimes the inverse of the route length between the ants’ nest and the food [27],
2. the amount of pheromone $F^{i-j}(t)$ accumulated on the path between i and j at time t on an ants path [28].

These two factors incentivize each agent to select a short path used by many ants reinforcing its use further. Inspired by nature, it is proposed in [28] to gradually evaporate the pheromone on all routes:

$$F^{i-j}(t+1) = (1 - \zeta) \cdot F^{i-j}(t) , \quad (1)$$

where $0 < \zeta < 1$ denotes a constant evaporation rate to be chosen in advance. As a consequence, routes which are chosen by fewer ants tend to fade faster over time until finally, one path emerges as the preferred path. In contrary to the algorithms stated above, our aim is not finding the shortest path, but separating points which belong to potentially low-dimensional manifold structures embedded in high-dimensional noisy points clouds. To achieve the goal, we introduce a novel ant colony strategy including a directional preference to move to points aligned with dominating directions of their local neighborhood enabling the discovery of manifolds, as detailed in the following.

2.1 Alignment based ant colony algorithm

We consider a data set $\mathcal{D} = \{\mathbf{x}_1, \mathbf{x}_2, \dots, \mathbf{x}_n\}$ of n points $\mathbf{x}_i \in \mathbb{R}^D$. For points in D -dimensional space, there are D principle components in $\mathcal{N}_r^{(i)}$, a neighborhood with radius r centered at point \mathbf{x}_i . Denote the local eigenvectors and eigenvalues by \mathbf{v}_d and λ_d for $d = 1, 2, \dots, D$, respectively. When jumping from \mathbf{x}_i to one of its neighbors $\mathbf{x}_j \in \mathcal{N}_r^{(i)}$, we would like to give higher preference to jumps along the dominant eigen-directions (\mathbf{v}_d with high λ_d). Local PCA performed on $\mathcal{N}_r^{(i)}$ yields, under the assumption of distinct eigenvalues, unique unit eigenvectors (up to possible direction flips indicated by opposite signs). We quantify the alignment of the jump vector $(\mathbf{x}_j - \mathbf{x}_i)$ with \mathbf{v}_d through their angle $\alpha_d^{(i,j)}$, in particular $|\cos \alpha_d^{(i,j)}|$. The alignment values are then normalized over all dimensions to give relative weighting of the alignment of $(\mathbf{x}_j - \mathbf{x}_i)$ with the eigen-directions by

$$w_d^{(i,j)} = \frac{|\cos \alpha_d^{(i,j)}|}{\sum_{d'=1}^D |\cos \alpha_{d'}^{(i,j)}|} . \quad (2)$$

Likewise, we express the relative importance of different eigendirections through normalized eigenvalues

$$\bar{\lambda}_d^{(i)} = \frac{\lambda_d^{(i)}}{\sum_{d'=1}^D \lambda_{d'}^{(i)}} . \quad (3)$$

¹Code and material available at <https://github.com/abst0603/LAAT>

We now define the preference for moving from \mathbf{x}_i to \mathbf{x}_j as

$$E^{(i,j)} = \sum_{d=1}^D w_d^{(i,j)} \cdot \bar{\lambda}_d^{(i)}, \quad (4)$$

meaning that it is more desirable to jump from \mathbf{x}_i to \mathbf{x}_j if $(\mathbf{x}_j - \mathbf{x}_i)$ is aligned with dominant eigendirections. We normalize this preference within $\mathcal{N}_r^{(i)}$ (the neighborhood of \mathbf{x}_i) resulting in the relative preference:

$$\bar{E}^{(i,j)} = \frac{E^{(i,j)}}{\sum_{j' \in \mathcal{N}_r^{(i)}} E^{(i,j')}}. \quad (5)$$

Considering the example of uniform or Gaussian noise, which exhibits roughly equal eigenvalues in all directions, the equations (4) and (5) result in higher probabilities of jumping to manifold points since they will provide the dominant eigen-directions aligned with the structure. This process gradually motivates the concentration of pheromone on the points alongside the manifold, rather than the points in background noise.

We define a slightly modified notion of the biologically inspired pheromone with $F^j(t)$ being the amount of pheromone accumulated at point \mathbf{x}_j at time t . The relative pheromone is normalized within the local neighborhood of \mathbf{x}_i :

$$\bar{F}^j(t) = \frac{F^j(t)}{\sum_{j' \in \mathcal{N}_r^{(i)}} F^{j'}(t)}. \quad (6)$$

In contrast to earlier approaches, we refrain from pheromone being released on the path between pairs of points in favor of its accumulation on the nodes itself. For our application this has two advantages: it is straightforward to reason which points may belong to a manifold based on the amount of the pheromone on them, and it is computationally more efficient.

We now combine the alignment with the pheromone to define the movement preference from \mathbf{x}_i to \mathbf{x}_j of an ant by:

$$V^{(i,j)}(t) = (1 - \kappa)\bar{F}^j(t) + \kappa\bar{E}^{(i,j)}. \quad (7)$$

The parameter $\kappa \in [0, 1]$ tunes the relative importance of the influence of the alignment and pheromone terms. In analogy with statistical physics, we view the jump preferences $V^{(i,j)}(t)$ as negative “energies” associated with the jumps and express the jump probabilities as:

$$P(j|i, t) = \frac{\exp(\beta V^{(i,j)}(t))}{\sum_{j' \in \mathcal{N}_r^{(i)}} \exp(\beta V^{(i,j')}(t))}, \quad (8)$$

where $\beta > 0$ plays the role of the inverse “temperature”.

We now summarize the proposed ant algorithm for the detection of potentially low-dimensional manifolds embedded in high-dimensional point clouds (see Algorithm 1 for the pseudo code). Hyper-parameters such as the number of ants N_{ants} , epochs N_{epoch} and steps N_{steps} are chosen according to the available memory and computation resources of the user. Intrinsic parameters to be selected are the neighborhood radius r , β , κ and φ , and ζ . They allow data and application specific tuning to structures the user is interested to find. They are very robust in practice as shown in section 4. Then, the local neighbors of \mathbf{x}_i are detected, and we compute local PCA for each point and save the results to save computational cost (see section 2.3. To urge the ants to start a path from a denser neighborhood the random starting points should satisfy:

$$|\mathcal{N}_r^{(i)}| > \tilde{\mathcal{S}} \quad (9)$$

Algorithm 1 The proposed ant colony algorithm for locating manifolds inside high-dimensional noise data points

Input: Data points, N_{epoch} , N_{ants} , N_{steps} , r , φ , ζ , β , κ
 $F^i(0) = 1 \forall \mathbf{x}_i \in \mathcal{D}$ and initialize the parameters

for $i = 1, \dots, n$ **do**

Find the local neighborhood $\mathcal{N}_r^{(i)}$ for \mathbf{x}_i .

Compute local PCA for each point.

Remove \mathbf{x}_i if $|\mathcal{N}_r^{(i)}| < d$.

end for

Compute the $\tilde{\mathcal{S}}$.

for $c = 1$ to N_{epoch} **do**

Place ants on random points as defined in (9)

for $k = 1, \dots, N_{\text{ants}}$ **do**

for $s = 1, \dots, N_{\text{steps}}$ **do**

From current node i select next node j with probability as defined in (8)

end for

Update pheromone as defined in (10)

end for

Apply evaporation as defined in (1)

end for

return \mathbf{F} containing the amount of pheromone on nodes

here $\tilde{\mathcal{S}}$ denotes the median of the set $\mathcal{S} = \{|\mathcal{N}_r^{(i)}| \mid \mathbf{x}_i \in \mathcal{D}\}$. Every ant performs a random walk on points from \mathcal{D} based on jump probabilities (8) for N_{steps} . The indices of the visited points by ant k are stored in the route multiset $R^{(k)}$. At the end of the walk the pheromone is updated according to:

$$F^j(t) = F^j(t-1) + \nu(j)\varphi, \quad \forall j \in R^{(k)}, \quad (10)$$

where φ denotes the constant amount of pheromone deposited on a point visited by an ant and $\nu(j)$ is the multiplicity of element j in multiset $R^{(k)}$.

A central part of the method is pheromone evaporation based on (1) that is applied to all points (rather than the path connecting them) after all ants finish their routes attaching pheromone at each step on each visited notes. Equation (8) with $\kappa \neq 1$ exhibits a reinforcing dynamic that gradually increases the probability to visit manifold nodes and hence the amount of pheromone accumulated on them in comparison to noise points. While pheromone evaporation attenuates the amount on all the points it enhances this reinforcement since it lessens the visitation probability for rarely visited points.

2.2 Comparison with Markov Chain

In our proposed ant algorithm the agents release pheromone on their way jumping from node i to j with a probability determined by two weighted terms: the alignment term based on the eigen-vectors and values in the local neighborhood of \mathbf{x}_i and the pheromone accumulated on the nodes from previous visits. The latter barring the consequence that the probabilities (8) change over time. However, if the ants ignore the pheromone ($\kappa = 1$) their next step just depends on the direction of the principal components in the local neighborhood and thus the transition probabilities will stay constant over time. This special case can be considered as a Markov Chain (MC) with a fixed transition matrix and can be studied as a stationary distribution over the point cloud. Therefore, the probability of jumping

from point (state) x_i to another one x_j is determined by $\overline{E}^{(i,j)}$ independent of the time t , and hence each state only depends on the previous state:

$$P(j|i) = \frac{\exp(\beta \overline{E}^{(i,j)})}{\sum_{j' \in \mathcal{N}_r^{(i)}} \exp(\beta \overline{E}^{(i,j')})}. \quad (11)$$

Therefore, the probability of jumping from point x_i to x_j is higher than jumping to x_k if the difference vector $x_j - x_i$ is more aligned with the main eigenvector than $x_k - x_i$ is.

If the neighborhood radius is large enough the set of points in our dataset will form a recurrent class, so that a path exists between any pair of points in the neighborhood graph. Under some additional assumptions, the point cloud can be identified with an ergodic Markov Chain (EMC) [29] characterised by the transition matrix $P_{ij} = P(j|i)$. In case the point cloud is organised in several isolated point clusters, we will have a set of distinct EMCs that can be analysed in isolation.

One key property of an EMC is that it converges to a steady-state which does not depend on the starting point, but only depends on the constant probabilities of jumping between the points [29]. Therefore, an EMC will converge to the steady state vector, which contains asymptotic visitation frequencies of all states (points). This steady-state vector π is the dominant left eigenvector of the transition matrix [29] and we have for all initial states i :

$$\lim_{s \rightarrow \infty} P_{ij}^s = \pi_j, \quad (12)$$

where P^s is the s -th power of P and P_{ij}^s is the probability of jumping from point i to point j in s steps. The transition matrix P grows quadratically in size with the number of points and therefore the computation of the eigenvectors quickly becomes computationally prohibitive to calculate for large datasets. Therefore, we take advantage of the Power method for computing the left dominant eigenvector [30]. This vector contains the visitation frequency for each point and assuming manifold points are more frequently visited we infer which points are more likely to belong to a manifold by thresholding.

The idea of discovering the underlying manifold inside a point cloud using a MC has previously been presented for dimensionality reduction and clustering applications [8, 13, 18, 31]. Those papers define the transition matrix according to a distance measure on the data capturing dense regions independent on dominant directions and alignments of manifolds. In contrast the aforementioned definition captures directional information of the data, which can reveal manifold structures embedded in large amounts of noise points in high dimensions. In the following sections we explain the synthetic and astronomical data to analyze and compare the performance of LAAT with state-of-the-art alternatives.

2.3 Computational complexity of LAAT

The complexity of the LAAT algorithm depends on the number of data points n , their dimensionality D , and the choice of the hyperparameters. The latter involves a data dependent component, namely the number of points in the neighborhood $|\mathcal{N}_r^{(i)}|$ with radius r of each sample x_i . We will state the worst-case upper bound with $\Delta = \max_i |\mathcal{N}_r^{(i)}|$ being the maximum number of neighbors for radius r . Equations (2)-(5) can be computed as a preprocessing step to reduce computational complexity at the cost of memory as implemented in algorithm 1. The neighborhoods are naively computed in $O(n^2 D)$, which can be sped-up using approximate techniques, such as [32]. For each neighborhood of maximum Δ points, local PCA is computed using singular value decomposition which is computed

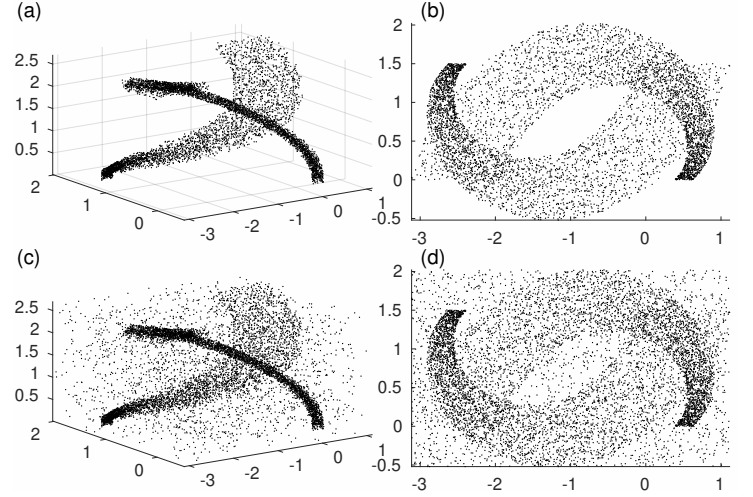


Figure 1: 3D (a,c) and front views (b,d) of the two-arm dataset, shown without (top) and with background noise (bottom).

in $O(\Delta^2 D + D^3)$ flops. The complexity also depends on the particular implementation as we use [33], however, in this section we only state the general case. Therefore the preprocessing amounts to $O(n^2 D + n(\Delta^2 D + D^3 + \Delta D^2))$. Lastly, the costs of the iterative procedure is maximally $O(N_{\text{epoch}} N_{\text{ants}} N_{\text{steps}} \Delta)$.

3 Data

To further investigate our proposed method, we conduct several experiments on real-world astronomical and synthetic datasets. As the central application for this method, we apply our technique to the cosmic-web [1] in which the galaxies and dark matter are distributed non-uniformly on many 1 and 2-dimensional manifolds (filaments and walls respectively).

3.1 Synthetic data

Two synthetic datasets are designed with similar challenges as real datasets, namely highly curved manifolds, with varying density on the manifolds itself (two-arms dataset), and multi-manifolds with different density. They serve for comparison of LAAT with existing methods and parameter analysis.

Two-arms This dataset contains two non-intersecting two-dimensional noisy arms curving in three dimensions positioned similar to a double helix embedded in 6000 three-dimensional uniform noise points (see Fig. 1). The design is loosely based on the form of astronomical objects such as tidal tails in galaxies, or ram pressure stripped gas wakes in cluster disk galaxies. Therefore, the distribution of the 3000 points of each arm is most dense at the narrow end, denoting the most recent position of the object, and decreases along the path where the particles have spread along a plane curved and tilted in space. To add to the complexity, the two manifolds contain noise with deviation from the 2D surface, such that the thickness of the arms is not zero. Specifically, uniform noise $U[0, 0.2]$ in orthogonal direction to the manifolds is added.

Cylinders This dataset contains four non-intersecting cylinders comprised of 1000 points each with varying height and diameter,

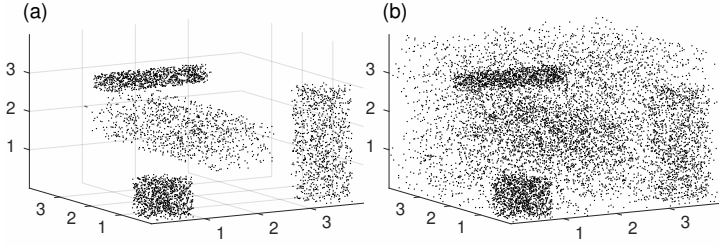


Figure 2: Four 3D cylinders of varying density shown without and with uniform background noise (panel a and b).

resulting in a vastly different density for each of them. The radii of two vertical cylinders are equal but their heights are different. 5000 data points with a uniformly random distribution are inserted as background noise to the dataset. No orthogonal "thickness" noise was added to the manifolds. Fig. 2 visualizes the dataset before and after adding the background noise in panel (a) and (b) respectively.

3.2 Data from a Cosmological N-body simulation

On mega-parsec scales, galaxies, galaxy clusters, and dark matter are not uniformly distributed in space. Due to the presence of small perturbations in the density-field of the early Universe, gravity later accumulates matter into a variety of large scale structures, including walls (which are flat, plane-like structures), filaments (which are long thin structures that arise where walls cross each other), and clusters (which are more spherical clumps of matter, arising where filaments cross, and that form some of the densest cosmological environments). Astronomers also observe gigantic and roughly spherical under-dense regions, called voids, containing few galaxies, whose boundaries are defined by the walls [1, 34]. In order to study how galaxy evolution is connected to their location in this large scale structure, it is necessary to identify the filaments, walls and clusters either observationally, or in large volume N-body cosmological simulations.

Figure 3 shows an example datacube of such a simulation. Our example simulation consists of 6.7 millions data points in a cube with edge size of $120h^{-1}\text{Mpc}$. Similar to observed galaxies the points

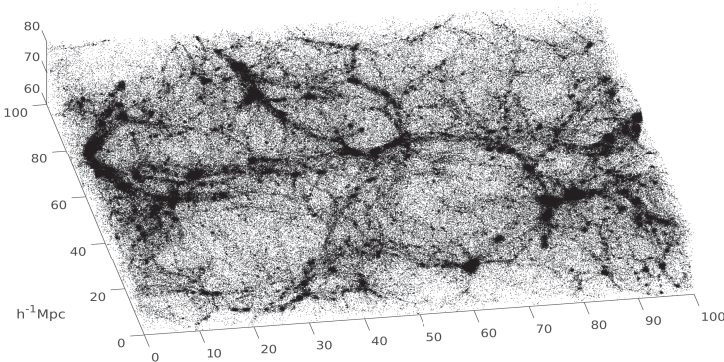


Figure 3: 810K particles from a cosmic-web simulation.

accumulate on a web-like structure composed of multiple filaments, walls and void structures, with varying sizes and densities. In such an N-body simulation, the complexity of the structure means there is no single, trivial way to define which particles belong to which large

scale structures. As a result, there is no "ground-truth" 100% correct answer to the question which particle belongs to which structure. This is a disadvantage for comparing our algorithm to other methods, which is mitigated by an additional experiment.

To construct controlled experiments of this kind, we use three synthetic datasets with low-dimensional substructures that look similar to those in the full cosmological simulation. These were first introduced in [10] and are based on Voronoi Tessellation regions that mimic cosmological voids. Walls build the faces of the tessellation regions, which form filaments on the edges where they meet. Finally clusters are found at the corners where filaments meet, such that similar structures appear as can be observed in cosmological simulations. In contrast to the n-body simulations these synthetic data sets provide a ground-truth, allowing to identify exactly which data points are associated with a particular structure. Note that the structures only appear morphologically similar to those in cosmological simulations and that they are unlikely to reproduce their more quantitative properties. Nevertheless, this enables us to quantify the relative performance of various methods for indentifying substructures that, at least, broadly resemble those found in cosmological simulations.

Three synthetic datasets are generated each consisting of 262,144 particles formed by Voronoi tessellation around 32 centers inside a cube with an edge length of $200h^{-1}\text{Mpc}$. The ratio of the number of points on filaments and clusters to walls and voids for datasets 'A', 'B', and 'C' is 0.367, 1.324, and 6.254, respectively. The cube of dataset 'A' is presented in Fig. 4. In contrast to N-body simulations points in this idealised model for cosmological structures distribute uniformly on each filament, yet their distribution varies across filaments.

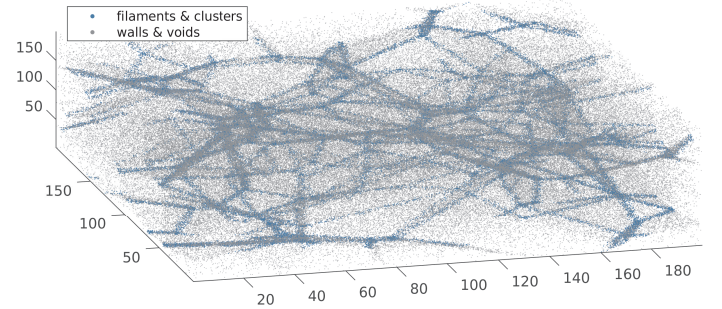


Figure 4: Synthetic cosmic-web acquired by Voronoi tessellation.

4 Experiments and discussion

In this section, we first present a quantitative evaluation measure for an objective comparison of techniques recovering manifolds from a noisy medium in the presence of ground truth, namely the Hausdorff distance. Subsequently, we perform an empirical analysis of the parameters of the proposed LAAT algorithm based on the synthetic datasets as introduced before, and we investigate the benefit of pheromone in the procedure of detecting the manifolds. Finally, we compare LAAT quantitatively with a known method in astronomy for detecting filaments over synthetic cosmic-web data and finally qualitatively on a large n-body simulation of the cosmic-web.

4.1 Average Hausdorff distance

The Hausdorff distance (HD) measures how far away from each other two non-empty sets X and Y in \mathbb{R}^D :

$$d_H(X, Y) = \max \left(\sup_{y \in Y} \left(\inf_{x \in X} \|x - y\| \right), \sup_{x \in X} \left(\inf_{y \in Y} \|x - y\| \right) \right) \quad (13)$$

Here, we use the Euclidean distance between two points x and y , which of course more generally could be any other distance [35]. HD measures the largest of all distances between points on one set to their nearest neighbor in the second set. Nonetheless, because the HD computes the supremum of the distance among points, it is sensitive to outliers. To overcome this disadvantage, the authors in [36] have suggested calculating the average distance instead of the maximum of the supremum distance. For two sets X and Y that contain N_X and N_Y number of points respectively, the average Hausdorff distance (AHD) is defined:

$$d_{AH}(X, Y) = \frac{\sum_{y \in Y} \left(\inf_{x \in X} \|x - y\| \right)}{2N_Y} + \frac{\sum_{x \in X} \left(\inf_{y \in Y} \|x - y\| \right)}{2N_X} \quad (14)$$

consisting of two distinguished averaging parts with each part computing a one-side average distance between the two sets. The smaller the values for the Hausdorff distance become the closer the two sets are. Therefore, we use the AHD for datasets where we have a ground truth to compute how close the set of points Y recovered from a noisy background by a manifold learning technique is to the true set of manifold points X .

4.2 Numerical Experiments on Synthetic datasets

4.2.1 Influence of LAAT parameters

In this experiment, we investigate the influence of the parameters on the final results of the LAAT algorithm. Parameters have mutual effect, such as κ , which determines the influence of the alignment and pheromone term, meaning the trade-off between following major directions versus reinforcing previous occupation, and β which tunes the transition probabilities. Similarly, the effect of the amount of pheromone released by an ant is coupled to the evaporation rate. Therefore we empirically demonstrate the influence of these important parameters of LAAT performing a systematic parameter grid analysis using the two-arms dataset consisting of manifolds of varying density introduced before.

The amount of pheromone accumulated on the data samples is used to decide which points belong to a manifold or can be considered background noise. In real-world applications, including discovering filaments in the cosmic-web, one should therefore select a single value for the whole data as a threshold on the amount of pheromone on the points guided by domain knowledge. However, in this experiment, to make a fair examination of the results we derive a strategy to select the threshold and follow the same strategy for all ten repetitions of the LAAT strategy. To do so, we build a calibration set that contains the same two manifolds as the two-arm dataset with different background noise, namely 6000 new random points in the medium around the two manifolds as noise. For each repetition of the experiment with the same parameter setting we perform the following two steps: 1) We first apply the LAAT strategy on the calibration set where the threshold on the resulting pheromone values is gradually reduced from maximum to the minimum across all points computing

the AHD for each, respectively. 2) The calibrated threshold value depicting the minimal AHD for the current parameter setup is then used as fixed threshold for all ten iterations on the original two-arm dataset. All parameters are initialized by the default values, namely $\beta = 10$, $\kappa = 0.5$, $\varphi = 0.05$, $\zeta = 0.1$, $N_{\text{epoch}} = 100$, $N_{\text{ants}} = 100$, and $N_{\text{steps}} = 2500$. Note that for the experiments of figure 5 panel (a) and (c), only the values of κ and β are changing, and in figure 5 (b) and (d), we alter the values of pheromone and the evaporation rate. The resulting mean AHD and its standard deviation for the parameter couplings κ and β are shown in the left column of figure 5 (panel (a, c)), while corresponding values for the pheromone and evaporation rate are depicted in panel (b, d).

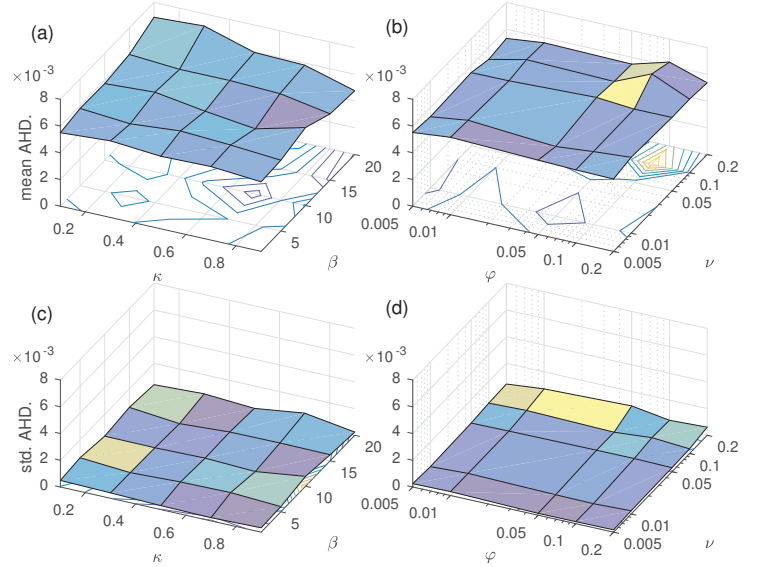


Figure 5: Two-arms: mean AHD and its standard deviation for parameter settings β and κ (panel a, c) and pheromone value versus evaporation rate (panel b, d) over 10 LAAT repetitions.

Figure 5 illustrates that the LAAT strategy recovers the underlying manifolds very well indicated by low AHD to the ground truth. It is furthermore robust against changing the β and κ (see panel (a) and (c)) in the range which the experiments were performed. There are points on the surface (a) corresponding to $\beta = 10$ and $\kappa = 0.7$, which depicts the lowest AHD with 4.8×10^{-3} on this dataset, however the difference to other settings is extremely small. For β larger than 20, the ants take a greedy policy following nearly exclusively the highest preference for the next jump, which generally results in larger standard variation across different repetitions and inclusion of more noise points away from manifolds. On the other hand, for β smaller than 1 the ants decide randomly, thus more noise points survive after applying the threshold. By increasing the value of κ from 0.1 to 0.9 for almost all values of β the AHD decreases, which indicates that the alignment is more important than the pheromone for detecting the manifolds with high curvature and varying noise as displayed by the two-arms dataset.

Figure 5 (b) and (d) demonstrate the effect of changing the pheromone amount φ and evaporation rate ζ in the range $[0.005, 0.2]$. Again the algorithm is very robust to changes in these parameters, since over the range which the experiment was performed it converges in all ten iterations to manifolds with very similar AHD. We observe that the amount of the deposited pheromone on each point increase by almost the same ratio for all points if we increase the φ ,

which does not have a large influence on the final results. For evaporation rate ζ values larger than 0.2 the ants make more random decisions as the pheromone on all points evaporates more quickly, resulting in higher standard deviation.

4.2.2 Benefits of pheromone

In this section we demonstrate the benefits of the inclusion of pheromone using the four-cylinder dataset with multiple manifolds of varying density compared to the background noise as introduced before. The pheromone serves as positive feedback reinforcing the chance of points on the manifold to get selected, since every time one ant visits a point it deposits extra pheromone on it and therefore motivates more ants to choose the same point. As stated in section 2.2 for the special case of the ants not depositing any pheromone or ignoring it when deciding about their next step each jump is dependent on just the former one and the process can be analyzed as MC. In other words, the special case of $\kappa = 1$ can be seen as MC including alignment information. Therefore, it is straightforward to prove that an EMC with a single class will converge to a steady state. However, as long as there are multiple classes in a dataset (multiple manifolds), such as the four-cylinder dataset, MC cannot always converge revealing all classes.

Informally, the neighborhood radius influences the number of neighboring points around one ant that can be the next step of the ant. Thus, if the neighborhood is large, then there is a small chance for every point to get selected. As a result, the ants' decision will be more irregular, which finally leads to a noisy output. In this experiment, both the ant colony algorithm and the MC with the transition matrix based on alignment are compared for three different values of the radius of the neighborhood (namely 0.3, 0.4 and 0.5) on the four-cylinders dataset. To do this, we fix the parameters for the LAAT strategy to default values and correspondingly $\beta = 10$ for the MC. For the LAAT strategy we examine the behavior of ten independent runs while the MC result, being the vector of the steady-state of the system, can be computed analytically.

Figure 6 illustrates the AHD on a logarithmic scale versus an increasing number of points remaining for all possible thresholds on the two deciding quantities, namely the amount of pheromone in LAAT and the steady-state vector corresponding to the visitation frequency in MC. In figure 6(a-c) reducing the threshold causes the number of points which survive to increase gradually, and the AHD continuously decreases until it reaches its minimum value, then it begins to increase monotonically until the threshold is smaller than the value of pheromone on all the points. The minimum AHD value for all LAAT runs and MC is found in the interval [4k 6k] exceeding the 4000 real manifold points, indicating that background noise, which is not on the manifolds is detected as well. As it is shown in the figures 6, the AHD between the ground truth and recovered manifolds is lower for the ant colony algorithm than MC on these three experiments for a range of thresholds which reveals that LAAT generally recovers the manifolds better including less noise points.

There are some sharp declines in the value of AHD in all figures, which corresponds to the discovery of the first point found on a new manifold. Figure 6 illustrates that the sharp declines happen faster in all LAAT runs than MC with the same radius of neighborhood. Since there are four cylinders with different sizes and densities inside the dataset, the MC with a transition matrix calculated based on a fixed radius (red lines in figure 6) cannot converge on all of them. To examine whether this is correct, we used the knowledge from ground truth about the position of points on or near to a cylinder. The new transition matrix was computed using different distances

for the neighborhood of different points according to the knowledge we have from ground truth. If a point is near to or on the cylinder with the smallest radius, the neighborhood radius was set to 0.2. For the two cylinders with the same radius, the neighborhood radius was set to 0.3, and for the rest of the points including the cylinder with the largest radius, the value was set to 0.3, 0.4, and 0.5. We therefore inform the MC which radius to use in which part of the dataset. As presented in the figure, the results of the informed MC are more similar to the results of ants, which shows that the ant colony algorithm with pheromone effect resembles the MC with altering radii. However, since the information about the position and number of manifolds buried in a noisy environment is typically not known in advance the ant colony algorithm, despite being computationally more expensive, is a very practical choice for unsupervised robust discovery.

4.2.3 Convergence analysis of LAAT

In this section, we investigate the convergence of the LAAT on the two-arm and four-cylinder datasets. All parameters are initialized by the default values. The whole experiment is then iterated ten times. At each epoch, the threshold is selected automatically on a second dataset which contains similar manifolds but different random noise similar to the strategy which is described in the previous section. Figure 7 shows that the LAAT quickly converge to the final mean AHD in just 10 epochs (see zoomed region) on both datasets. As is stated in algorithm 1, an epoch is started by sending ants one after another to explore the data points, and it is finished by pheromone evaporation. We furthermore notice the very small standard deviation across the independent runs indicating that although ants start from random points every epoch, all ants visit the manifold points more often and hence accumulate more pheromone there.

4.2.4 Synthetic dataset that broadly mimics cosmological structures (Synthetic cosmic-web)

One proposed technique for identifying filaments inside the cosmic-web used by astronomers is the publicly available Disperse [11, 12]. Disperse builds a Delaunay tessellation field estimator density for each point. Then, using discrete Morse theory and theory of persistence it finds the clusters, filaments, and the walls and measures their different strengths. We compare the performance of the proposed LAAT method with Disperse on the three synthetic cosmic-web datasets [10] (see 3.2). The difference between these datasets is the ratio of the number of particles on filaments and clusters (labeled as positive) as well as walls and voids (labeled as negative).

To compare the ant colony algorithm for manifold denoising with disperse we follow the same experiments as suggested in [10], since the methods have different parameters. Disperse, for example, has a significance parameter (number of σ) which corresponds to the strength of the detected structure to the noise. Moreover, Disperse returns lines to resemble the found filaments and it does not convey any information about its thickness. Therefore, as suggested by [10], we identify the points which are located within a fixed radius around the detected filament line as points on the filament. The solid lines in figure 8 present the performance in terms of Precision and Recall of Disperse for several significance values ($n\sigma$) and various radius sizes around the filament lines.

For the LAAT method, all parameters have been set to default values for all experiments, and the radius of neighborhood is set to 0.3. The only parameter which is altered is the threshold applied on the deposited pheromone on each point. We select the threshold

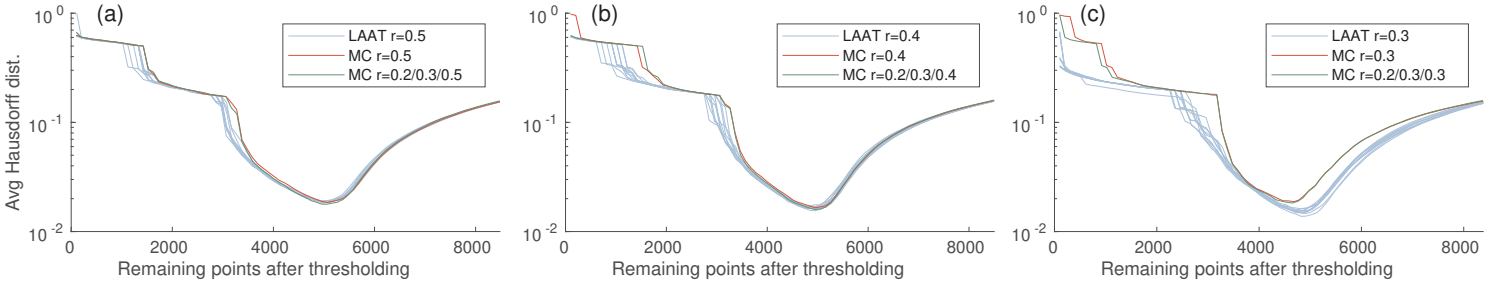


Figure 6: AHD curves for the ant colony algorithm, MC, and MC with altering radii. Panels (a-c) show LAAT and MC performance with fixed neighborhood radius equal to 0.5, 0.4 and 0.3, respectively, and MC with altering radii as mentioned in the legend.

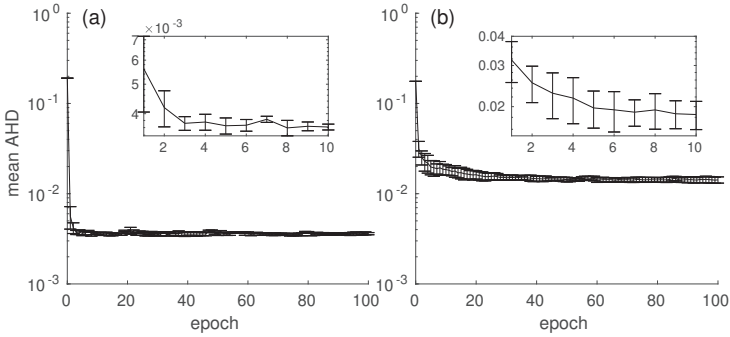


Figure 7: Ants mean AHD curve of the (a) two-arm and (b) four-cylinder data and zoomed boxes showing epoch 1 to 10.

value such that the number of remaining points is the same as the number of points after choosing a fixed strength value and fixed radius for Disperse. This process is iterated for several strength values and radii. The dashed lines in figure 8 present the results of LAAT on the three synthetic cosmic-web datasets with ground truth. Figure 8 illustrates as the number of positive labels increases from dataset A to C, the performance of both methods improves. Nonetheless, in most cases, with the same number of the survivor points as the output of Disperse and LAAT, both the precision and recall rates are higher for our method. In Fig. 8 panel (c) as the number of false negatives goes to zero, the recall rate reaches to one for 3σ , 4σ , and 5σ strength values. At this stage, the points which are labeled positive by Disperse include almost all the dataset points. However, since some of these points are seldom visited by ants, the amount of pheromone on many of them are almost the same and near to zero. Thus by applying a threshold on the result of LAAT, all the points in the dataset are selected, and the precision suddenly jumps to the lowest value possible.

Figure 9 demonstrates the result of LAAT and Disperse applied to dataset A (see Figure 4). For Disperse the strength value is fixed to 6σ and the resulting filament lines are visualized in red. The gray points denote the surviving points after applying the threshold to the LAAT result. Figure 9 shows that Disperse did not reveal several even relatively strong filaments for this strength value. Moreover, it sometimes produces fake filaments in places where there are no actual filaments in the dataset, mostly near the borders. Although few points on the walls (labeled as noise) surviving after applying the threshold, the LAAT successfully discovers most filaments with few noise points.

4.3 Numerical comparison of LAAT, MC, and LLPD

To compare the LAAT, MC based on distance and alignment, and LLPD we investigate first based on the two-arm dataset. All these methods use a threshold to distinguish noise points from the points on the manifolds and therefore we compare them over the complete range of possible threshold values. The value was reduced from the maximum possible on a point to the minimum for each method, and the AHD between the surviving points after thresholding and the ground truth was computed. LAAT does not provide an analytical solution and thus we repeated the experiment 10 times and visualized the results of all three methods separately (see figure 10). Remarkably the AHD for LAAT is lower than the other methods for almost the entire range. LLPD performs better each time it discovers the first points on a denser part of the arms until reaching roughly 5000 points. Then, as more and more points are recovered with increasing thresholds, more and more noise points survive in comparison to other techniques, clearly shown by comparably high AHDs. Interestingly, MC with a transition matrix based on alignment outperforms MC based on the distance between points, but only slightly. This indicates that the alignment information is useful for detecting manifold with curvature.

Table 1 summarizes the AHD results on two synthetic datasets for the four methods. We determine the threshold for LLPD by obtaining the knee point in the plot of path distance to the 20th nearest neighbor as recommended in [13]. For the other three methods, we select the threshold of the lowest AHD on the calibration dataset as is described before and apply the same threshold on the pheromone value on each point for LAAT, or on the vector which represents the steady-state situation of MC. Next, we compute the AHD between surviving points and ground truth. For LAAT the whole procedure was repeated ten times, and the number presents the mean value over all iterations. Table 1 reveals that LAAT outperforms the other methods over two datasets as it depicts the lowest AHD compared to the three other methods. The AHD on the two-arm dataset for MC with a transition matrix based on alignment information is lower than the distance based MC. Nonetheless, the results are different on the four-cylinder dataset, which might suggest that the alignment information plays a crucial rule in discovering manifolds with curvature. On the four-cylinders, the data points are spread uniformly in the volume, thus the jumping probabilities are similar in all directions. Hence, the performance of MC with alignment is similar to MC with distance.

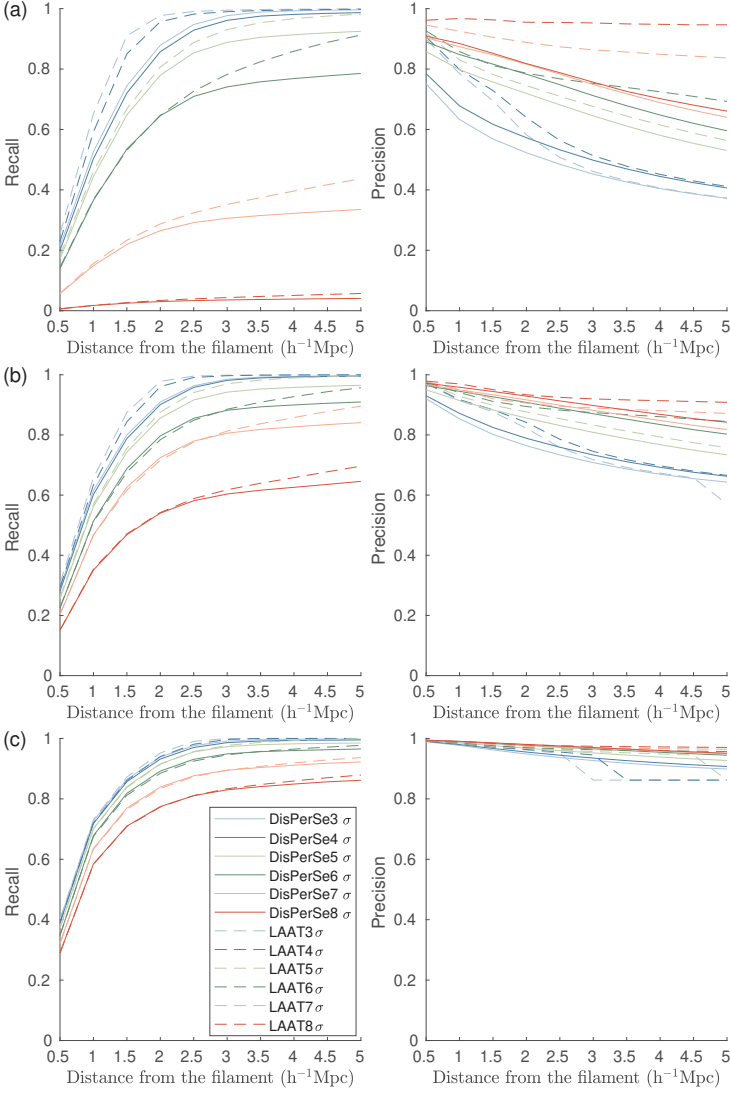


Figure 8: Precision and recall rates of the ant colony method with alignment versus Disperse for dataset A, B and C (a-c).

4.4 Comparison on N-body cosmological simulation

We will now apply LAAT to the problem of detecting filaments in cosmological simulations of the cosmic web. In particular, we will compare LAAT with a widely used method in astrophysics, Disperse. The methods are compared on the 6.7 million points real-world N-body simulation of the cosmic-web as illustrated in figure 3. For LAAT most parameters are kept at their previously mentioned default values while some are adapted to the data and application need. Specifically, we give more preference to the directional importance of the filaments and their one-dimensional nature by setting $\kappa = 0.8$ and the neighborhood radius is set to 0.5. Due to the large number of samples and observing that the density notably varies on the manifolds we increase the number of ants and steps to make sure they cover all parts of the data ($N_{\text{ants}} = 200$, $N_{\text{steps}} = 12000$) and adapt the strategy of the ants placement in each epoch. Instead of placing ants on random points to start their walk we divide the whole data into 200 smaller cubes and in each iteration a single ant is placed randomly in each of them. Due to the particularly steep

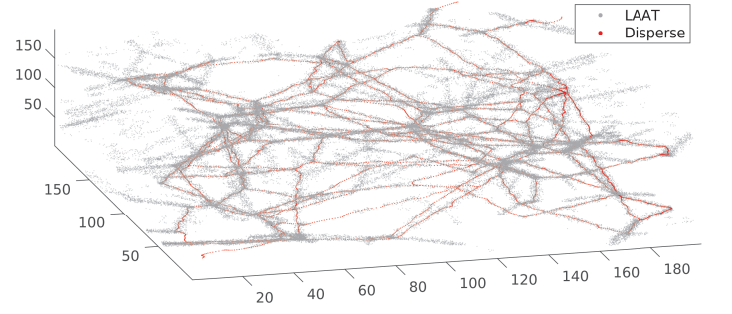


Figure 9: The results of LAAT and Disperse on dataset A

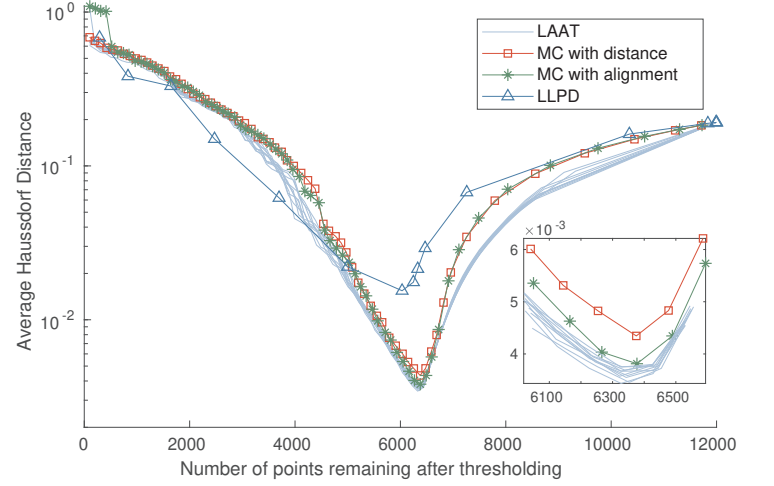


Figure 10: The AHD plots for LAAT, MC with alignment, MC with distance, and LLPD on two-arm dataset with 6000 points on arms. The small box illustrates a larger view of the plot when the number of survived points is between 6000 to 6600.

density gradient in this dataset it is hard for the ants to escape the high-density regions, which is not avoided completely by increasing the number of ants and steps. Therefore, to catch the hugely varying densities we apply LAAT on the whole data, select all points the ants put pheromone on, and then exclude these points for a rerun on the remaining points. For this data and setting LAAT consumes about 8.7GB of RAM and every epoch takes about 11 minutes to compute the pheromone vector over a single core of a 4.5GHz processor and the preprocessing step took roughly 4 hours. This can be reduced by parallelization as planned in future work.

Structures are identified by both methods LAAT and Disperse by a thresholding strategy based on the Pheromone and strength

Table 1: AHD of methods for two-arm and four-cylinder.

dataset	LAAT	MC (Alignment)	MC (Distance)	LLPD
Two-arm	$3.59 \cdot 10^{-3}$	$3.77 \cdot 10^{-3}$	$4.38 \cdot 10^{-3}$	$1.54 \cdot 10^{-2}$
Four-cylinder	$1.42 \cdot 10^{-2}$	$1.92 \cdot 10^{-2}$	$1.79 \cdot 10^{-2}$	$5.69 \cdot 10^{-2}$

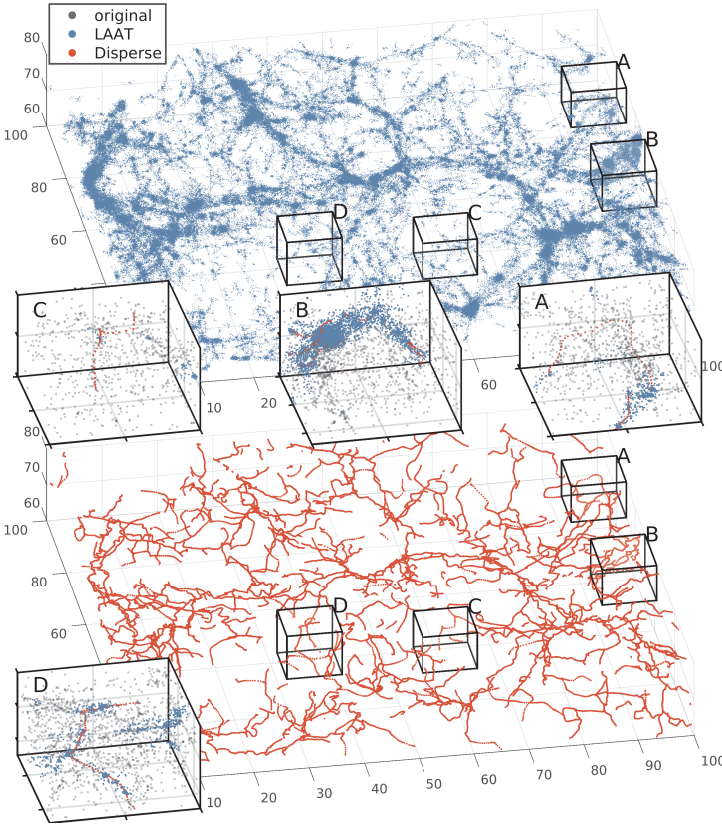


Figure 11: Results of LAAT and Disperse (top and bottom panel in blue and red) on the cosmic-web dataset. Zoomed regions show examples of: false positives introduced by Disperse (A and C), as well as a strong filament found by LAAT but mostly missed by Disperse (B). Cube D shows a rare occasion where Disperse detects a filament more clearly than LAAT.

parameter respectively. For LAAT our astronomical experts select an appropriate threshold for a small random cube covering 10% of the volume of the whole dataset, which is then subsequently used for the full dataset. The strength parameter for Disperse is also set by experts to 7σ . To make the filaments smoother each point is afterwards replaced by the mean of ten neighboring points within the same filament. For this setup of the experiment, Disperse took 4.5 hours on a 3.5GHz processor, and it occupies 80GB of RAM. Note that Disperse run-time increases drastically if the sigma value is decreased to show fainter filaments.

The results of both methods applied to the same data cube can be found in figure 11. Disperse detects many filaments inside the data, but also identifies filaments in places in which there are no or few sample points. Increasing the strength parameter decreases the appearance of false “ghost” filaments at the cost of missing others. Notably, LAAT detects filaments of largely varying thickness along the filament. Altering the threshold value over a range on all points reveals weaker filaments and points which are located on walls (two-dimensional manifolds) with much lower density structure than the filaments. The cubes A-D in figure 11 show zoomed regions that exemplify differences in the methods. Zoom B contains a quite strong and clear filament found by LAAT but disconnected and missed by Disperse. A and C show examples of “ghost” filaments introduced by Disperse in regions that do not appear to contain dense clear

structures in the original data or marked by LAAT. Rarely one can find filaments that are nicely marked by Disperse and appear more disconnected by LAAT as depicted in zoom D. The qualitative comparison between the widely used Disperse and LAAT illustrates the versatility of our method capable of finding weak structures as well as filaments with strongly varying density robustly.

5 Demonstration on high-dimensional data

While Liebeskind et al. [1] focus on large scale structures in 3D physical space, such as filaments of the cosmic web, astronomers are more and more frequently working with multi-dimensional data. An interesting higher dimensional problem to demonstrate the potential of LAAT is to help astronomers to detect star forming regions in galaxies. According to current theory star particles are created in regions of dense and cool gas and also high CII emission are associated with star formation [37]. The CII emission rate (in $\text{erg s}^{-1} \text{cm}^{-3}$) for each gas particle can be computed leveraging chemical evolution models of the galactic gas and taking into account its ionization equilibrium and ion level occupation [38, 39]. Thus in the following, we demonstrate LAAT on an simulation snapshot of a galaxy containing 6 dimensions, including the three dimensions for the position of the gas particles, their density ρ , temperature τ , and CII emission (photon emission at wavelength of $158 \mu\text{m}$ due to carbon ion C^+). Details on the physical models and simulation description used to obtain the galaxy snapshot under study, see [40].

We take advantage of these extra dimensions and incorporate them as reward terms in equation (7) as follows:

$$V^{(i,j)}(t) = \kappa_1 \bar{F}^j(t) + \kappa_2 \bar{E}^{(i,j)} + \kappa_3 \bar{\rho}^{(i,j)} - \kappa_4 \bar{\tau}^{(i,j)} + \kappa_5 \bar{\text{CII}}^{(i,j)}. \quad (15)$$

Here, $\bar{\tau}^{(i,j)}$ and $\bar{\text{CII}}^{(i,j)}$ are defined analogously to

$$\bar{\rho}^{(i,j)} = (\rho_j - \rho_i) / \left(\sum_{j' \in \mathcal{N}_r^{(i)}} |\rho_{j'} - \rho_i| \right). \quad (16)$$

The sign of temperature in (15) is negative, since the lower the temperature, the higher the chance of star formation. Figure 12 depicts the simulated galaxy in 3D space color coded with the physical quantities ρ , τ , and CII emission, respectively.

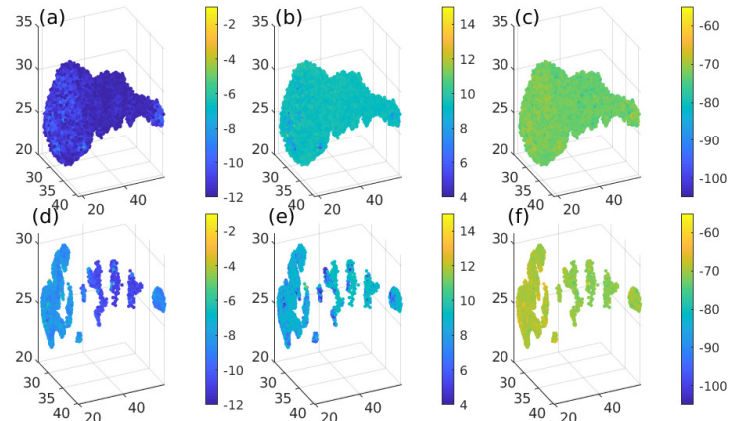


Figure 12: The color in a-d, b-e, and c-f pairs shows gas density, temperature, and CII in log scale, respectively. The second row of images(d, e, and f) illustrate the result of applying LAAT.

Here again, all parameters are set to default values except for $r = 0.7$, $N_{\text{epoch}} = 20$, and $\kappa_c = 0.2$ for all c in set $\{1, 2, \dots, 5\}$. The bottom row of figure 12 indicates that LAAT not only discloses points that belongs to manifolds but also make sure that these points satisfy the user-defined reward terms, namely high gas density, low temperature, and high CII emission which denote suitable conditions for star formation.

6 Conclusion

We propose the Locally Aligned Ant Technique (LAAT) to detect multiple manifolds buried in a large number of noise and outliers. The method is inspired by the heuristic ant colony algorithm extended by the incorporation of local alignment information and a reinforcing pheromone term. Section 2.2 details the relationship to the Markov Chain which can be considered a special case of LAAT when no pheromone is released. We quantitatively demonstrated and compared the performance of alternative techniques on several synthetic data sets of varying complexity evaluated empirically using the AHD to the underlying noiseless manifolds. The experiments reveal that LAAT performs similarly or superior to alternative methods, robustly detecting structures of high curvature, varying density and even finding multiple manifolds with distinct features simultaneously. Additionally, we illustrate our method on two large real-world astronomical datasets. A 6.7 million point N-body simulation of the cosmic-web which is qualitatively compared to a technique widely used by astronomical experts. Unlike [11, 12], and [10] our method can naturally deal with more than three dimensions, and we demonstrate how experts can use extra information in the form of reward terms to prescribe properties of structures to detect.

Acknowledgement



This project has received financial support from the European Union's Horizon 2020 research and innovation program under the Marie Skłodowska-Curie grant agreement No. 721463 to the SUNDIAL ITN network.

We thank the Center for Information Technology of the University of Groningen providing access to the Peregrine high performance cluster.

References

- [1] N. I. Libeskind, R. van de Weygaert, M. Cautun, B. Falck, E. Tempel, T. Abel, M. Alpaslan *et al.*, “Tracing the cosmic web,” *Mon Not R Astron Soc (MNRAS)*, vol. 473, no. 1, pp. 1195–1217, Jan. 2018.
- [2] M. E. Sardi, J. M. Gilmore, B. Groppe, L. Florens, and M. P. Washburn, “Identification of Topological Network Modules in Perturbed Protein Interaction Networks,” *Scientific Reports*, vol. 7, p. 43845, Mar. 2017.
- [3] P. G. Camara, “Topological methods for genomics: Present and future directions,” *Curr Opin Syst Biol*, vol. 1, pp. 95–101, Feb. 2017.
- [4] B. Y. Torres, J. H. M. Oliveira, A. T. Tate, P. Rath, K. Cumnock, and D. S. Schneider, “Tracking Resilience to Infections by Mapping Disease Space,” *PLOS Biology*, vol. 14, no. 4, p. e1002436, Apr. 2016.
- [5] J. L. Nielson, S. R. Cooper, J. K. Yue, M. D. Sorani, T. Inoue, E. L. Yuh, P. Mukherjee, T. C. Petrossian, J. Paquette, P. Y. Lum *et al.*, “Uncovering precision phenotype-biomarker associations in traumatic brain injury using topological data analysis,” *PLOS ONE*, vol. 12, no. 3, p. e0169490, Mar. 2017.
- [6] F. Chazal, B. Fasy, F. Lecci, B. Michel, A. Rinaldo, and L. Wasserman, “Subsampling Methods for Persistent Homology,” in *Proc Int Conf Mach Learn (ICML)*, F. Bach and D. Blei, Eds., vol. 37. Lille, France: PMLR, Jul. 2015, pp. 2143–2151.
- [7] S. T. Roweis and L. K. Saul, “Nonlinear dimensionality reduction by locally linear embedding,” *Science*, vol. 290, no. 5500, pp. 2323–2326, Dec. 2000.
- [8] S. Wu, P. Bertholet, H. Huang, D. Cohen-Or, M. Gong, and M. Zwicker, “Structure-Aware Data Consolidation,” *IEEE Trans Pattern Anal Mach Intell*, vol. 40, no. 10, pp. 2529–2537, Oct. 2018.
- [9] M. Hein and M. Maier, “Manifold Denoising,” in *Advances in Neural Information Processing Systems 19*, B. Scholkopf, J. C. Platt, and T. Hoffman, Eds. MIT Press, 2007, pp. 561–568.
- [10] N. Shivashankar, P. Pranav, V. Natarajan, R. v. d. Weygaert, E. P. Bos, and S. Rieder, “Felix: A Topology Based Framework for Visual Exploration of Cosmic Filaments,” *IEEE Trans Vis Comput Graph*, vol. 22, no. 6, pp. 1745–1759, Jun. 2016.
- [11] T. Sousbie, “The persistent cosmic web and its filamentary structure I: Theory and implementation,” *Mon Not R Astron Soc (MNRAS)*, vol. 414, no. 1, pp. 350–383, Jun. 2011.
- [12] T. Sousbie, C. Pichon, and H. Kawahara, “The persistent cosmic web and its filamentary structure II. Illustrations,” *Mon Not R Astron Soc (MNRAS)*, vol. 414, no. 1, pp. 384–403, Jun. 2011.
- [13] A. Little, M. Maggioni, and J. M. Murphy, “Path-Based Spectral Clustering: Guarantees, Robustness to Outliers, and Fast Algorithms,” *Journal of Machine Learning Research*, vol. 21, no. 6, pp. 1–66, 2020.
- [14] A. Y. Ng, M. I. Jordan, and Y. Weiss, “On Spectral Clustering: Analysis and an algorithm,” in *Adv Neural Inf Process Syst*, T. G. Dietterich, S. Becker, and Z. Ghahramani, Eds. MIT Press, 2002, pp. 849–856.
- [15] S. Deutsch and G. G. Medioni, “Intersecting Manifolds: Detection, Segmentation, and Labeling,” in *IJCAI*, Buenos Aires, Argentina, 2015.
- [16] D. Gong, X. Zhao, and G. G. Medioni, “Robust Multiple Manifold Structure Learning,” in *ICML*, 2012.
- [17] R. R. Coifman and S. Lafon, “Diffusion maps,” *Applied and Computational Harmonic Analysis*, vol. 21, no. 1, pp. 5–30, Jul. 2006.
- [18] P. D. Dixit, “Introducing user-prescribed constraints in markov chains for nonlinear dimensionality reduction,” *Neural Computation*, vol. 31, no. 5, pp. 980–997, May 2019.
- [19] Y. Saad, *Numerical Methods for Large Eigenvalue Problems*, revised edition ed. Philadelphia: SIAM e-books, May 2011.
- [20] J. Valencia-Aguirre, A. lvarez Meza, G. Daza-Santacoloma, C. Acosta-Medina, and C. G. Castellanos-Domnguez, “Multiple Manifold Learning by Nonlinear Dimensionality Reduction,” in *Iberoamerican Congress on Pattern Recognition (CIARP)*, ser. LNCS, C. San Martin and S.-W. Kim, Eds., vol. 7042. Berlin, Heidelberg: Springer, 2011, pp. 206–213.
- [21] M. Dorigo, G. Di Caro, and L. M. Gambardella, “Ant algorithms for discrete optimization,” *Artificial Life*, vol. 5, no. 2, pp. 137–172, 1999.
- [22] L. M. Gambardella and M. Dorigo, “Solving symmetric and asymmetric TSPs by ant colonies,” in *Proceedings of IEEE International Conference on Evolutionary Computation*, May 1996, pp. 622–627.
- [23] Cheng-Fa Tsai, Han-Chang Wu, and Chun-Wei Tsai, “A new data clustering approach for data mining in large databases,” in *Proc. Int. Symp. Parallel Archit. Algorithms Networks*, May 2002, pp. 315–320.
- [24] X.-y. Liu and H. Fu, “An Effective Clustering Algorithm With Ant Colony,” *Journal of Computers*, vol. 5, no. 4, pp. 598–605, Apr. 2010.
- [25] S.-C. Chu, J. F. Roddick, C.-J. Su, and J.-S. Pan, “Constrained Ant Colony Optimization for Data Clustering,” in *PRICAI 2004: Trends in Artificial Intelligence*, ser. LNCS, C. Zhang, H. W. Guesgen, and W.-K. Yeap, Eds. Springer Berlin Heidelberg, 2004, pp. 534–543.
- [26] R. Pless and R. Souvenir, “A survey of manifold learning for images,” *IPSP Trans Comput Vis Appl*, vol. 1, pp. 83–94, Jan. 2009.

- [27] M. Dorigo, “Optimization, Learning and Natural Algorithms,” PhD Thesis, Politecnico di Milano, Italy, 1992.
- [28] M. Dorigo and G. Di Caro, “The ant colony optimization meta-heuristic,” in *New Ideas in Optimization*, D. Corne, M. Dorigo, F. Glover, D. Dasgupta, P. Moscato, R. Poli, and K. V. Price, Eds. Maidenhead, UK, England: McGraw-Hill Ltd., UK, 1999, pp. 11–32.
- [29] C. M. Grinstead and J. L. Snell, *Introduction to Probability*, 2nd ed. Providence, RI: American Mathematical Society, Jul. 1997.
- [30] R. Larson, B. H. Edwards, and D. C. Falvo, *Elementary Linear Algebra*, 5th ed. Houghton Mifflin, 2004.
- [31] S. Steinerberger, “A filtering technique for Markov chains with applications to spectral embedding,” *Applied and Computational Harmonic Analysis*, vol. 40, no. 3, pp. 575–587, May 2016.
- [32] S. Arya and D. M. Mount, “Approximate range searching,” *Computational Geometry*, vol. 17, no. 3, pp. 135–152, Dec. 2000.
- [33] G. Guennebaud, B. Jacob *et al.*, “Eigen v3,” eigen.tuxfamily.org, 2010.
- [34] E. Platen, R. Van De Weygaert, and B. J. T. Jones, “A cosmic watershed: the WVF void detection technique,” *Mon Not R Astron Soc (MNRAS)*, vol. 380, no. 2, pp. 551–570, Sep. 2007.
- [35] J.-D. Boissonnat, F. Chazal, and M. Yvinec, *Geometric and Topological Inference*. Cambridge University Press, 2018.
- [36] M. Dubuisson and A. K. Jain, “A modified Hausdorff distance for object matching,” in *Proc of 12th ICPR*, vol. 1, Oct. 1994, pp. 566–568 vol.1.
- [37] I. De Looze, M. Baes, G. J. Bendo, L. Cortese, and J. Fritz, “The reliability of [C II] as an indicator of the star formation rate,” *Mon Not R Astron Soc (MNRAS)*, vol. 416, no. 4, pp. 2712–2724, Sep. 2011.
- [38] U. Maio, K. Dolag, B. Ciardi, and L. Tornatore, “Metal and molecule cooling in simulations of structure formation,” *Mon Not R Astron Soc (MNRAS)*, vol. 379, no. 3, pp. 963–973, Aug. 2007.
- [39] S. De Rijcke, J. Schroyen, B. Vandenbroucke, N. Jachowicz, J. Decroos, A. Cloet-Osselaer, and M. Koleva, “New composition-dependent cooling and heating curves for galaxy evolution simulations,” *Mon Not R Astron Soc (MNRAS)*, vol. 433, no. 4, pp. 3005–3016, Aug. 2013.
- [40] R. Verbeke, E. Papastergis, A. A. Ponomareva, S. Rath, and S. De Rijcke, “A new astrophysical solution to the too big to fail problem,” *Astronomy & Astrophysics*, vol. 607, p. A13, Oct. 2017.